Cement and Concrete Research 159 (2022) 106900

Contents lists available at ScienceDirect

Cement and Concrete Research

journal homepage: www.elsevier.com/locate/cemconres

The nanomechanical properties of non-crosslinked calcium aluminosilicate hydrate: The influences of tetrahedral Al and curing age

Jiaqi Li [a,*], Wenxin Zhang [b], Paula Sanz-Camacho [c], Mathieu Duttine [c], David Gardner [d], Carlo Carraro [d], Roya Maboudian [d], Thomas Huthwelker [e]

[a] Atmospheric, Earth, and Energy Division, Lawrence Livermore National Laboratory, 94550, United States
[b] Division of Engineering and Applied Science, California Institute of Technology, Pasadena 91125, United States
[c] CNRS, Univ. Bordeaux, Bordeaux INP, ICMCB UMR 5026, F-33600 Pessac, France.
[d] Department of Chemical and Biomolecular Engineering, University of California, Berkeley 94720, United States
[e] Paul Scherrer Institut, Swiss Light Source, Villigen, Switzerland

ARTICLE INFO

Keywords:
C-A-S-H
C-S-H
High-pressure X-ray diffraction
Bulk modulus
Blended cement

ABSTRACT

Calcium aluminosilicate hydrate (C-A-S-H) is the binding phase of both blended cement-based and alkali-activated materials. The intrinsic mechanical properties of non-cross-linked C-A-S-H are important while experimentally unvalidated. Here, the properties are for the first time measured using high-pressure X-ray diffraction. The incompressibility and bulk modulus K_0 of C-A-S-Hs are correlated to their nanostructure and stability using nuclear magnetic resonance and X-ray absorption spectroscopies. Al coordination in stable C-A-S-H (Al/Si = 0.1) cured for 546 days is purely tetrahedral (Al^{IV}), while in metastable C-A-S-H (Al/Si = 0.05) cured for only 182 days is both Al^{IV} and pentahedral (Al^{V}). The stable C-A-S-H is stiffer along the a,b,c-axis with higher K_0 relative to C-S-H. Short-curing-induced metastable C-A-S-H (Al/Si = 0.05) shows expanded interlayer and softer c-axis, thus lower K_0 than C-S-H and the stable C-A-S-H. Our results highlight the stiffening effect of Al^{IV} incorporation and the negative influences of insufficient curing on the nanomechanical properties of non-cross-linked C-A-S-H at Ca/Si = 1.

1. Introduction

The most used supplementary cementitious materials (SCMs) include coal fly ash, ground granulated blast-furnace slag (GGBFS), natural pozzolan, and calcined clay [1]. These SCMs are mainly amorphous (calcium) aluminosilicate, used as substitutes for Portland cement clinker or ordinary Portland cement (OPC) [2]. SCMs are primarily used to enhance the durability of concrete, increase the long-term mechanical properties of concrete, reduce CO_2 emissions associated with concrete production, and/or improve the workability of fresh concrete [3–5].

The binding phase of blended-cement concrete is nanocrystalline calcium aluminosilicate hydrate (C-A-S-H) [6]. The binding phases of alkali-activated materials (e.g., alkali-activated GGBFS and Ca-rich coal fly ash), lime-based mortar, and ancient Roman concrete are also C-A-S-H or C-A-S-H like [7–11]. C-A-S-H is highly mesoporous and often foil-like at the submicron scale [12–14]. C-A-S-H is structurally similar to calcium silicate hydrate (C-S-H) at the nanoscale, the primary binding phase of OPC [15]. The atomic structures of both C-S-H and C-A-S-H can be described as an analog to a defective tobermorite [16–18], which contains CaO_7 sheets flanked with (alumino)silicate chains and charge-balancing ions and water in the interlayer. At elevated synthesis temperatures (e.g., >80 °C), the C-A-S-H nanostructure is highly similar to Al-tobermorite with Al incorporated at cross-linking sites [19]. When the synthesis condition is room temperature, C-A-S-H is commonly non-cross-linked [20]. Al with different types of coordination environments in non-cross-linked C-A-S-H have been proposed: tetrahedrally coordinated Al (Al^{IV}) at the bridging sites of aluminosilicate chains [21–23]; pentahedrally coordinated Al (Al^{V}) possibly charge-balanced in the interlayer or at bridging site [23–26]; and octahedrally coordinated Al (Al^{VI}) possibly in the interlayer or at bridging site, or appears as a separate phase—the third aluminate hydrate (TAH) [21]. A recent study suggested that the hotly debated TAH does not exist as a separate phase, and this Al^{VI} species is within the structure of C-A-S-H [27].

Understanding the mechanical properties of C-A-S-H at different scales is of great significance for optimizing the mechanical properties of many construction materials (e.g., blended cement-based materials and

* Corresponding author at: Lawrence Livermore National Laboratory, 7000 East Avenue, Livermore, CA 94550, United States.
E-mail address: li88@llnl.gov (J. Li).

https://doi.org/10.1016/j.cemconres.2022.106900
Received 19 September 2020; Received in revised form 24 June 2022; Accepted 1 July 2022

alkali-activated materials). The micromechanical properties of C-A-S-H have been intensively studied using nanoindentation [9,28–30]. However, the results obtained from nanoindentation are sensitive to many factors (e.g., surface roughness, packing density, and intermixed phases) [28,31–33]. Moreover, our recent studies have shown that high deviatoric stresses result in structural distortion and preferred orientation of C-S-H and C-A-S-H nanocrystallites [34–36]. Thus, results from nanoindentation can not accurately represent the intrinsic mechanical properties of randomly orientated C-A-S-H nanocrystallites. High-pressure X-ray diffraction (HP-XRD) has been proved as a reliable tool for determining the mechanical properties of (nano)crystalline cement-related phases at the unit-cell scale [37]. In HP-XRD studies, mesopores in powder samples can be filled with a pressure-transmitting medium [38,39]. Thus, hydrostatic pressure is applied to the sample grains, and the intrinsic mechanical properties of samples at the unit cell scale can be measured using HP-XRD. Unlike nanoindentation studies [29,33], where reports may reflect the mechanical properties of intermixed multi-phase assemblages, HP-XRD can probe the mechanical properties of the unit cell of a single phase in phase assemblages.

Our recent HP-XRD studies have shown the correlations between the nanomechanical properties and the nanostructure of (Al-)tobermorite, C-S-H, and cross-linked C-A-S-H: 1) the compressibility along the a- and b- axes (i.e., the basal plane) is independent of the Ca-to-Si molar ratio (Ca/Si) of C-S-H [39,40]; 2) the c-axis (normal to the basal plane) compressibility of C-S-H and tobermorite is governed by the interlayer density (i.e., the c-axis is stiffer at a higher interlayer density) [40,41]; and 3) the cross-linking sites decrease the compressibility of C-A-S-H and tobermorite along the c-axis (i.e., cross-linking sites result in a stiffer interlayer) [38]. Understanding the nanomechanical properties of non-cross-linked C-A-S-H is even more important because non-cross-linked C-A-S-H is more common in hardened cement at ambient temperature relative to cross-linked C-A-S-H [20]. However, the influences of Al incorporation on non-cross-linked C-A-S-H are complex and remained unexplored due to the facts: 1) at low Ca/Si molar ratios (e.g., <1.0) or when the curing age is short, the ordering of C-A-S-H is low (no basal peak), thus making HP-XRD measurements challenging; 2) Al^{IV}, Al^{V}, and/or Al^{VI} may co-exist in C-A-S-H at higher Ca/Si ratios [23,42]; and 3) different types of Al coordination environment may co-exist in a metastable C-A-S-H structure at low Ca/Si ratios when the curing age is short [26]. Thus, it is important to decouple the influences of different types of Al coordination environments on the intrinsic mechanical properties of non-cross-linked C-A-S-Hs. Moreover, previous studies have suggested that the equilibrium of C-A-S-H takes a few months under room temperature synthesis conditions and the chemical composition and nanostructure vary over time before equilibrium [42–44]. Understanding the influences of Al^{IV} and phase stability (affected by curing age) is the first but critical step to further decouple the Al coordination influences on the intrinsic mechanical properties of non-cross-linked C-A-S-Hs.

In this study, the intrinsic mechanical properties of two batches of non-cross-linked C-A-S-Hs at a molar Ca/Si ratio of 1.0 are measured using HP-XRD: 1) a stable structure with only Al^{IV} at Al/Si = 0.1 after a long curing age (546 days); 2) a metastable structure with mainly Al^{IV} and minor Al^{V} at Al/Si = 0.05 after a short curing age (182 days). Al and Si coordination environments of the samples are determined using ^{27}Al nuclear magnetic resonance (NMR) spectroscopy and X-ray absorption near-edge structure (XANES) spectroscopy, respectively. A correlation between the nanostructure and nanomechanical properties (intrinsic mechanical properties at the unit cell scale) of non-cross-linked C-A-S-Hs is found. The results are highly impactful in validating theoretical calculations of nanomechanical properties of C-A-S-H (e.g., from molecular dynamics and density functional theory), developing forcefield in simulations, further decoupling the influences of different Al coordination environments, and designing concrete using bottom-up approaches.

2. Materials and methods

2.1. Materials

Non-cross-linked C-A-S-H samples were synthesized at an initial bulk Ca/Si of 1.0 and initial bulk Al-to-Si molar ratios (Al/Si) of 0.05 and 0.1. Stoichiometric amounts of $CaO{\cdot}Al_2O_3$, fumed SiO_2 (Aerosil 200, Evonik), and CaO (from calcined $CaCO_3$) were mixed with deionized water at a water-to-solid mass ratio of 45 in a N_2-filled glove box. The C-A-S-H samples with Al/Si of 0.05 and 0.1 were cured for 182 days and 546 days, respectively, at 20 °C. This curing temperature favors the formation of non-cross-linked C-A-S-H. However, a long curing age is needed for the formation of an evident (002) peak, the index for unit cell parameter *c*, and the stability of the C-A-S-H structure [43]. Higher temperatures could accelerate the synthesis but favor the formation of cross-linked C-A-S-H or tobermorite. After vacuum filtration, the wet samples were freeze-dried for seven days. The dry powders were equilibrated in N_2-filled desiccators at 30 % relative humidity, then sealed in vacuum bags until analyses. For more synthesis details, see [45].

The high Al sample was cured longer because C-A-S-H with higher Al content often requires a longer time to show an evident (002) peak in XRD. Otherwise, the lack of an evident (002) peak would make our nanomechanical properties impossible. The HP-XRD probes over a million C-A-S-H unit cells and is a bulk measurement of intrinsic mechanical properties that needs no nanoindentation-like probability analysis. Unlike nanoindentation, HP-XRD is independent of mesopores influences. Thus, one load of each C-A-S-H sample is adequate for nanomechanical properties measurement. The long curing age (equilibrium by 546 days, evidenced in [43]) suggested that the Al/Si = 0.1 sample is stable. A sample with lower Al content but cured also for 546 days is unnecessary in this study, because 1) our previous HP-XRD studies of C-S-Hs, cross-linked C-A-S-H, and different tobermorite structures confirm that two samples are adequate for understanding one compositional/structural influencing factor in a comparison study; 2) we have already studied a reference, non-cross-linked C-S-H at Ca/Si = 1 prepared using the same protocol and precursor batch [39]; and 3) an additional non-cross-linked C-A-S-H sample with a weak (002) peak requires long precious beamtime.

To understand the nanomechanical properties of metastable non-cross-linked C-A-S-H, a relatively short curing age of C-A-S-H is required. Preliminary results showed that a 20 °C-cured C-A-S-H with Ca/Si = 1.0 and Al/Si = 0.1 at 182 days lacks the (002) peak for our HP-XRD study due to the relatively high Al content and short curing age. Thus, a non-cross-linked 182-day-cured C-A-S-H at Al/Si = 0.05 with an evident (002) peak was selected in this study. This sample has not reached equilibrium as suggested in [42–44]. This curing age is equivalent to that of the aforementioned C-S-H reference at Ca/Si = 1.0 [39]. Other non-cross-linked C-A-S-H samples are not suitable in this HP-XRD study due to 1) the absence of (002) peak; 2) additional variable; and 3) the incorporation of a mixture of Al^{IV}, Al^{V}, and Al^{VI} at higher Ca/Si ratios [45], which would be challenging for decoupling the Al influences. In summary, the selected two samples at Ca/Si = 1.0 are sufficient to study the two factors (Al^{IV} incorporation and structural metastability) in the nanomechanical properties of non-cross-linked C-A-S-H.

2.2. Method

2.2.1. X-ray diffraction

The XRD experiment was conducted at the superbend beamline 12.2.2 of the Advanced Light Source (ALS) at the Lawrence Berkeley National Laboratory. The incident X-ray beam energy was 25 keV (corresponding wavelength of 0.4979 Å), and the beam spot size was ~30 μm. MAR345 image plate was used as a detector for collecting 2D diffraction images. The sample-to-detector distance was ~332 mm. These measurements were conducted at room temperature. The

exposure time for each scan was 960 s. For ambient pressure measurement, the powder samples were loaded into glassy capillaries.

For high-pressure measurements, we used a BX-90 diamond anvil cell (axial geometry), including a pair of brilliant-cut diamonds with a culet diameter of ~400 μm. A cylindrical chamber (100 μm × 100 μm) was drilled in a rhenium gasket using a laser-milling machine. 1–3 ruby spheres (0.05 wt% Cr^{3+}-doped α-Al_2O_3) and lightly packed C-A-S-H powders were loaded into the chamber. Subsequently, methanol-ethanol solution (4:1 by volume), a pressure transmitting medium, was poured into the chamber using a small syringe. The chamber was immediately sealed by the pair of diamond anvils. The ruby spheres, acting as a pressure gauge (error < ±0.15 GPa), are used to indicate the applied hydrostatic pressure in the chamber [46]. Lattice parameters were refined using *CelRef* with Merlino's B11m tobermorite structure [47].

The axial Biot stain, ε, of the edge length (i.e., lattice parameters a, b, and c) of a unit cell is defined in Eq. (1):

$$\varepsilon = \frac{l - l_0}{l_0} \tag{1}$$

where l_0 and l are edge lengths of a unit cell at ambient pressure and at the applied hydrostatic pressure in the chamber, respectively.

The correlation between ambient pressure bulk modulus, K_0 (GPa), of a unit cell and its pressure-induced volumetric change of a cement-related (nano)crystalline phases can be described by the second-order Birch-Murnaghan equation of state (BM-EoS, Eq. (2)):

$$P = \frac{3}{2}K_0\left[(1-\varepsilon_v)^{-\frac{7}{3}} - (1-\varepsilon_v)^{-\frac{5}{3}}\right] \tag{2}$$

where P is the applied hydrostatic pressure indicated by the ruby spheres in the chamber (GPa) and ε_v is the volumetric strain of a unit cell.

2.2.2. Nuclear magnetic resonance spectroscopy

^{27}Al solid-state NMR spectra were recorded on a Bruker Avance 300 MHz spectrometer operating at magnetic field strength of 7.05 T corresponding to Larmor frequency of 78.204 MHz. ^{27}Al solid-state NMR experiments were carried out using a standard 4-mm Magic Angle Spinning (MAS) probes with MAS rates of 10 kHz. Chemical shifts are references relative to $Al(NO_3)_3$. A short pulse length of 1.3 μs corresponding to a selective π/2 pulse determined by using a $Al(NO_3)_3$ aqueous solution was employed. A recycle delay of 0.5 s was applied to both samples.

2.2.3. X-ray absorption near-edge structure spectroscopy

The XANES spectra at Ca $L_{2,3}$-edge were collected using the scanning transmission soft X-ray spectroscopy (STXM) at the beamline 5.3.2.2 at the ALS. The C-A-S-H samples at Al/Si = 0.1 was dispersed in 99 + % isopropanol under laboratory conditions, then dropped onto a Si_3N_4 membrane window (100 nm thick, Norcada). The window was mounted on the STXM sample stage at 1/3 atm. STXM was operated at a spatial resolution of 25 nm so that C-A-S-H foils and crystalline impurities, e.g., carbonates and aluminate, can be distinguished. The measurement was replicated for 30 times at an energy resolution of 0.1 eV.

The XANES spectra at Si K-edge were collected at the PHOENIX beamline (station II) at the Swiss Light Source at the Paul Scherrer Institute, Switzerland. The samples were lightly pressed onto thin indium foils, which were attached to a scratched copper plate. The spectra were obtained at an energy step of 0.2 eV for 1 s for each data point from a vacuum chamber. All data were collected using the fluorescence-yield mode with a 500 μm × 500 μm beam at room temperature.

3. Results and discussion

3.1. Ambient pressure structure

The diffractogram of C-A-S-H with Al/Si of 0.05 and 0.1 at ambient pressure is shown in Fig. 1. Only a trace amount of vaterite, a polymorph of $CaCO_3$, was observed in C-A-S-H (Al/Si = 0.1). Vaterite is less stable than calcite at room temperature. The presence of vaterite here is likely due to the extreme drying conditions (i.e., freeze-drying) [68]. Other secondary products, e.g., katoite, were not found in XRD patterns. Except for the (002) peak, the C-A-S-H samples showed comparable peak positions. The lattice parameters, a, b, and γ, of the two C-A-S-H samples are comparable and similar to the C-S-H counterparts at the same Ca/Si = 1 (see Table 1). The lattice parameter, *c*, of the two C-A-S-H samples is different and higher than that of the C-S-H reference with Ca/Si of 1. The Al-incorporation-induced expansion of basal spacing is consistent with existing literature [26,48]. A recent study suggests the curing-time effect on the stability of C-A-S-H also affects the basal spacing before equilibrium [42–44].

The ^{27}Al NMR spectra of C-A-S-H are shown in Fig. 2. For the Al/Si = 0.1 sample cured for 546 days, only Al^{IV} was observed in the spectrum, suggesting that all Al is at bridging sites of silicate chains. For the Al/Si = 0.05 sample cured for 182 days, the Al coordination environment is dominated by Al^{IV} at 61.5 and 52.8 ppm, while the secondary environments are Al^{V} at ~31.3 ppm and Al^{VI} at 11.3 ppm. Apparently, the content of Al^{V} and Al^{VI} is much lower than that of Al^{IV} in the Al/Si = 0.05 sample. The co-existence of Al^{V} and Al^{VI} in the Al/Si = 0.05 sample can be explained by a shorter reaction age, 182 days, compared to 546 days for the Al/Si = 0.1 sample. This observation is consistent with a previous study where only Al^{IV} was found in C-A-S-H at low Ca/Si and low Al/Si ratios for long-term curing while Al^{V} and/or Al^{VI} were observed for short-term curing [26]. Note that further quantification of the fractions of Al species is challenging in the present study, particularly at a low magnetic field, because of the asymmetric nature of the Al^{IV} resonance of poorly crystalline materials, most likely governed by a distribution in ^{27}Al quadrupole coupling parameters or chemical shifts [49]. This asymmetric nature of Al^{IV} resonance suggests the absence of Al^{V} of C-A-S-H (Al/Si = 0.1, 546 days), which is consistent with a previous study [26].

The Al^{VI} signal at 11.3 ppm is not attributed to TAH as the chemical shift of TAH is ~4 ppm in ^{27}Al NMR [21]. This Al^{VI} signal at 11.3 ppm has been suggested to originate from katoite [45] or a hydroxyl-AFm phase [50]; neither was detected by XRD—because 1) Al^{VI} only accounts for a very low fraction of total Al content; and 2) the low Al/Si ratio is only 0.05. The below-detection-limit crystalline Al^{VI} phases in XRD is consistent with [45]. The Al^{VI} signal (either katoite or hydroxyl-AFm) suggests that the C-A-S-H sample at Al/Si = 0.05 under this condition only contains Al^{IV} and Al^{V} within the unit cell. The long curing age, 546 days, at Al/Si of 0.1 favors the incorporation of purely Al^{IV} in a stable nanostructure. The relatively short curing age, 182 days, at Al/Si of 0.05, results in a metastable nanostructure [43], which incorporates Al^{V} in the interlayer or at bridging sites [25,48] in addition to Al^{IV}. C-A-S-H at Al/Si = 0.05 at 182 days has not reached equilibrium. Otherwise, the basal spacing of C-A-S-H at Al/Si = 0.05, if stable, should be lower than that of the stable C-A-S-H at Al/Si = 0.1. Thus, the significantly larger basal spacing of C-A-S-H at Al/Si = 0.05 is mainly attributed to

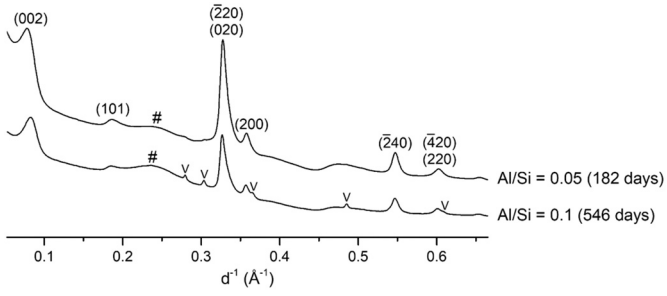

Fig. 1. Diffractogram of non-cross-linked C-A-S-Hs (Ca/Si = 1.0). The lattice planes of C-A-S-H are labeled. V: vaterite (<1 wt%). # diffraction of capillary.

Table 1
Lattice parameters and water contents of C-S-H and non-cross-linked C-A-S-H samples with Ca/Si = 1.0 under ambient conditions.

	Al/Si = 0 (182 days) [39]	Al/Si = 0.05 (182 days)	Al/Si = 0.1 (546 days)
a (Å)	6.65 ± 0.01	6.68 ± 0.01	6.70 ± 0.01
b (Å)	7.32 ± 0.01	7.31 ± 0.01	7.32 ± 0.01
c (Å)	22.1 ± 0.1	25.1 ± 0.2	24.0 ± 0.1
γ	122.8°	123.2°	123.1°
basal spacing (Å)	11.05	12.54	12.02
H_2O/Si[a]	1.2 ± 0.3	1.4 ± 0.3	1.5 ± 0.3

Lattice parameter c is twice of the basal spacing.
[a] Water content is obtained from thermogravimetry results in [42].

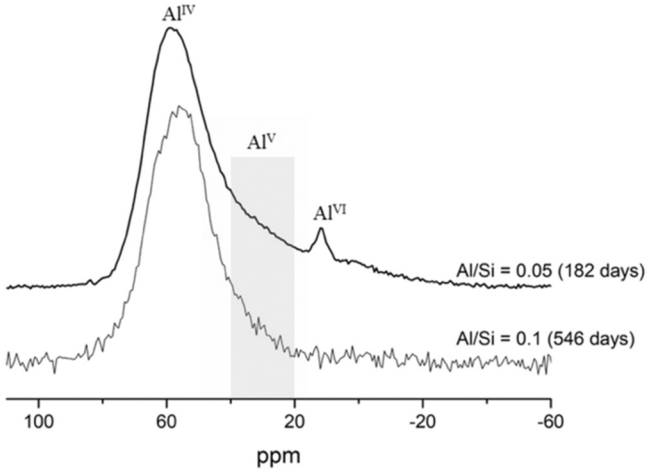

Fig. 2. ^{27}Al NMR spectra of non-cross-linked C-A-S-H (Ca/Si = 1.0). The Al/Si =0.05 sample shows a better signal-to-noise ratio due to its higher quantity for the measurement relative to the Al/Si =0.1 sample (limited available quantity). The enlarged plot for comparison is shown in Fig.S1 in Supplementary Information.

the metastable structure and metastability-induced Al^V. The presence of Al^V is also proof of the metastability of C-A-S-H at a low Ca/Si ratio at 182 days. Otherwise, the sample with lower Al content should contain only Al^{IV}, like the stable high-Al C-A-S-H at Al/Si = 0.1, which was cured for 546 days. The presence of non-TAH Al^{VI} signal is another proof of such metastability at low Ca/Si ratios. During the C-A-S-H synthesis, katoite formed initially from strongly oversaturated solutions as the silicon concentration was low [42]. As amorphous silica dissolved, the Al uptake in C-S-H developed at the expense of katoite. As the curing time increased from three months to three years, the katoite content systematically decreased in the C-A-S-H batches [43]. When the system with Ca/Si = 1.0 and Al/Si = 0.05 reached equilibrium, the dissolved calcium, aluminum, and hydroxide concentrations were stabilized and undersaturated with respect to crystalline phases (e.g., katoite) [42–44]. Thus, our mixed Al^{IV} and Al^V C-A-S-H sample at Al/Si = 0.05 at 182 days is metastable. This fact is consistent with the simulation in Mohamed et al. [27], where Al^V is always stable in almost all C-A-S-Hs with Ca/Si over 1.0 while Al^{IV} is stable at low Ca/Si ratios, e.g., 1.0.

Fig. 3 shows the XANES spectra of C-A-S-Hs and cross-linked tobermorite (double-chain) at the Si K-edge. Three absorption features (B, D, and E) are found in the spectra. The major peak B (Si K-edge) at ~1840 eV corresponds to the electron transition from 1s to 3p orbital of Si [51]. The minor peaks D and E are attributed to the multi-scattering effect from more distant atomic shells and the electron transition from 1s to 3d orbital, respectively. Our previous study has found that the energy position of peak B positively correlates to the degree of silicate polymerization of C-S-H, C-A-S-H, and (Al-)tobermorite [52]. The energy position

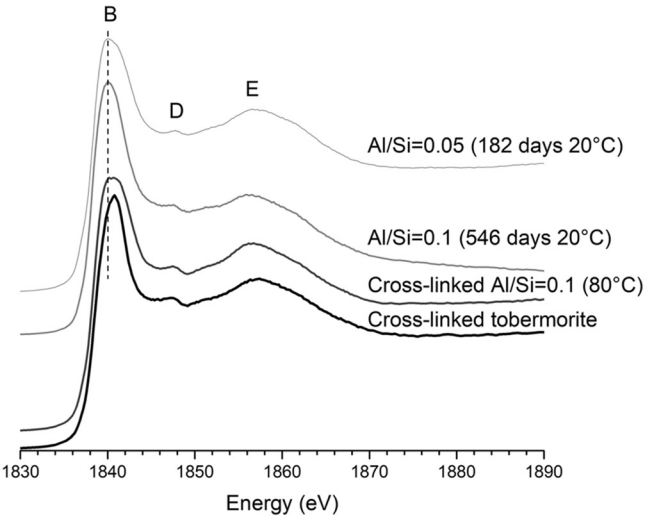

Fig. 3. XANES spectra of C-A-S-Hs and tobermorite at Si K-edge. The dash-line is an eye-guide of peak positions. The spectrum of cross-linked tobermorite is reproduced from [52]. The cross-linked structure of C-A-S-H (Ca/Si = 1.0 and Al/Si = 0.1) synthesized at 80 °C has been confirmed by ^{29}Si NMR in [19], where the synthesis conditions can be found.

of C-A-S-Hs (Al/Si of 0.05 and 0.1) synthesized at 20 °C is lower compared to that of two cross-linked silicates: 1) 11 Å tobermorite and 2) C-A-S-H (Ca/Si = 1.0 and Al/Si = 0.1) synthesized at 80 °C. This fact suggests that the C-A-S-Hs synthesized at 20 °C in the present study are non-cross-linked; otherwise, the two 20 °C C-A-S-H samples would exhibit similar energy positions of peak B compared to the cross-linked silicates. Cross-linked structure of C-A-S-Hs at similar Ca/Si ratio, Al/Si ratio, and curing age using the same raw materials is also not found in a paralleled study [43].

XANES spectra of the C-A-S-H samples at the Ca $L_{2,3}$-edge are shown in Fig. 4. The peaks a_1, a_2, b_1, and b_2 are critical in evaluating the symmetry of Ca—O coordination symmetry. They correspond to the electron excitation of Ca from the 2p to 3d orbital and crystal field splitting [53]. The peak positions of the two C-A-S-H samples are highly comparable. The energy differences, also known as splitting energies, between a_1 and a_2 and between b_1 and b_2 are 1.1 eV and 1.05 eV, respectively. These values of splitting energy are consistent with those of C-S-H and C-A-S-H from silicate hydration and different synthesis methods [13,40,54–56]. This range of splitting energies suggests a low

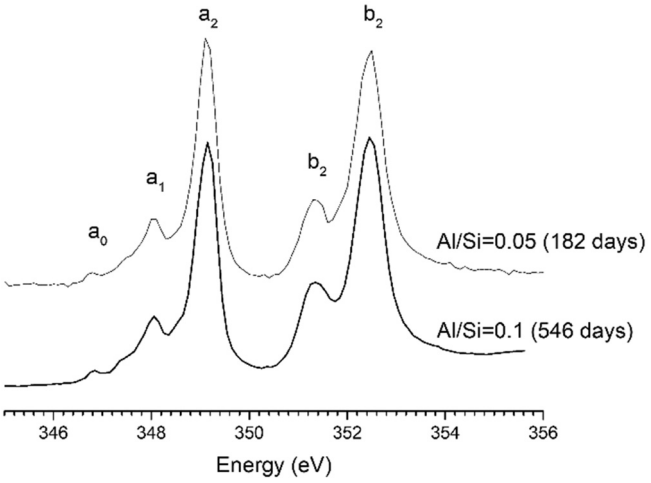

Fig. 4. XANES spectra of C-A-S-H (Ca/Si = 1.0) at Ca $L_{2,3}$-edge. The XANES spectrum for the Al/Si = 0.05C-A-S-H sample is reproduced from [13].

degree of carbonation of the C-A-S-H sample; otherwise, the splitting energy of carbonated C-S-H or C-A-S-H would often be ~1.2–1.35 eV [57].

3.2. High pressure XRD

X-ray diffractograms of non-cross-linked C-A-S-H with Al/Si of 0.05 and 0.1 as a function of applied hydrostatic pressure are shown in Fig. 5. As applied hydrostatic pressure increases, diffraction peaks with decreased intensity systematically shift to lower d-spacing, resulting from the pressure-induced contraction of unit cells. For example, the decreased d-spacing of (002) peak as applied hydrostatic pressure increases represents a pressure-induced closing of the interlayer region. The diffraction peaks in both C-A-S-H samples are more diffuse at higher hydrostatic pressure as the phases are disordered under pressure. This pressure-induced structural disorder is a common observation found in high-pressure studies of C-S-Hs and tobermorite, e.g., HP-XRD [41,58], high-pressure X-ray Raman [34], and high-pressure optical Raman [59]. The (002) peaks are most sensitive to the amorphization, indicating lower stability and ordering of the C-A-S-H nanostructure along the c-axis.

The axial incompressibility of non-cross-linked C-A-S-H along each axis is defined as the Biot strain along a-, b-, and c-axes as a function of applied hydrostatic pressure. The incompressibility along the a- and b-axes can be linearly fitted, as shown in Fig. 6A. The incompressibility is governed by the local structure of C-A-S-H. The incompressibility along the a- and b- axes of non-cross-linked C-A-S-H sample with Al/Si = 0.1 is about $-1/380$ GPa^{-1}, which is higher than the incompressibility of C-S-H at Ca/Si = 1.0, $-1/315$ GPa^{-1} [39] and cross-linked C-A-S-H at Ca/Si = 1.0, $-1/285$ GPa^{-1} to $-1/300$ GPa^{-1} [38]. The about 8–10 % longer Al—O bond in Al^{IV} coordination [60] relative to Si—O (e.g., 1.60–1.66 Å in C-S-H [61,62]) shows no negative influence on ab-planar incompressibility of non-cross-linked C-A-S-H at Al/Si = 0.1 with only Al^{IV}. The higher ab-planar (the basal plane) incompressibility of the non-cross-linked C-A-S-H Al/Si = 0.1 in the present study can be attributed to more interlayer Ca charge-balanced with bridging aluminate sites. The cross-linking site in our previous studies of cross-linked C-A-S-H [38] exhibits a hinge-like deformation around the shared O atom [41]; this reorientation of bonds, rather than bond contraction, requires lower energy [63]. Thus, cross-linked C-A-S-H at the same Ca/Si and Al/Si ratios in our previous study shows lower ab-planar incompressibility than non-cross-linked C-A-S-H in the present work. The ab-planar incompressibility of non-cross-linked C-A-S-H sample with Al/Si = 0.05 is similar to C-S-H at the same Ca/Si ratio of 1.0. This fact cannot be attributed to the major Al species, Al^{IV}, which stiffens ab-plane. The short-curing-induced metastable nanostructure at Al/Si = 0.05 compromises the stiffening effect of Al^{IV}. This fact might be related to a negative influence of metastable Al^{V} on C-A-S-H at Al/Si = 0.05. Al^{V}-O is substantially longer and weaker than Si—O (i.e., ~1.65 Å long) in C-S-H [61]. The average Al—O bond length of Al^{V} coordination, e.g., in andalusite [64], is 1.84 Å. In a stable nanostructure of C-A-S-H, higher local water content could stabilize Al^{V} due to the availability of oxygen for this higher coordination [27]. Al—O bond length of Al^{VI} coordination, e.g., in gibbsite [65], is ~1.91 Å. As more Al^{V} and Al^{VI} form at higher Ca/Si ratios [26], future HP-XRD studies will investigate non-cross-linked C-A-S-H with higher Ca and Al content to further validate the negative influence of long Al^{V}-O and/or Al^{VI}-O bonds on the ab-planar incompressibility of C-A-S-H.

Although the basal spacing of non-cross-linked C-A-S-H at Al/Si = 0.1 is 0.95 Å larger than C-S-H, the incompressibility along the c-axis of non-cross-linked C-A-S-H at Al/Si = 0.1 (see Fig. 6B) is slightly higher than that of C-S-H at Ca/Si = 1.0 in Geng et al. [39]. In Geng et al. [39], the c-axis of C-S-H is softer as the basal spacing increases. This trend is not observed in the present study because c-axis incompressibility directly correlates to interlayer density, not simply interlayer spacing [40]. The stiffer c-axis of stable C-A-S-H (Al/Si = 0.1) relative to C-S-H can be explained by a higher interlayer density of non-cross-linked C-A-S-H at Al/Si = 0.1 (i.e., more interlayer Ca needed for charge-balancing Al^{IV} than Si [41]). The c-axis incompressibility of non-cross-linked C-A-S-H at Al/Si = 0.1 in the present study is lower than that of cross-linked C-A-S-H at the same Ca/Si and Al/Si ratios, $-1/245$ GPa^{-1} [38], due to the influence of cross-linking sites, which withstand the pressure-induced closing of the interlayer. The lower c-axis incompressibility of non-cross-linked C-A-S-H at Al/Si = 0.05 relative to C-S-H at the same Ca/Si ratio of 1 is due to the short-curing-induced metastable with a non-optimal interlayer density: 1) a 1.5 Å larger basal spacing; and 2) less interlayer Ca to charge balance Al at the low Al/Si ratio of 0.05. Note that the lower c-axis incompressibility at Al/Si = 0.05 should not be simply assigned to the Al^{V} incorporation or Al coordination number.

The bulk modulus at ambient pressure, K_0, is fitted with the second-order BM-EoS (see Eq. (2)). K_0 is influenced by the local structure of C-A-S-H. The measured K_0 of non-cross-linked C-A-S-H at Al/Si = 0.1 is 82 ± 4 GPa (see Fig. 7), much higher than C-S-H at the same Ca/Si ratio of 1 (67 ± 1 GPa, prepared at the same temperature). This fact is due to the higher incompressibility along all axes of C-A-S-H at Al/Si = 0.1. The low K_0, 56 ± 2 GPa, of C-A-S-H at Al/Si = 0.05 is due to its low c-axis incompressibility (i.e., metastability-induced non-optimal low interlayer density) relative to stabilized C-S-H and long-curing-age C-A-S-H at Al/Si = 0.1. Note that the impurity katoite does not influence the intrinsic mechanical properties of C-A-S-H because HP-XRD measures

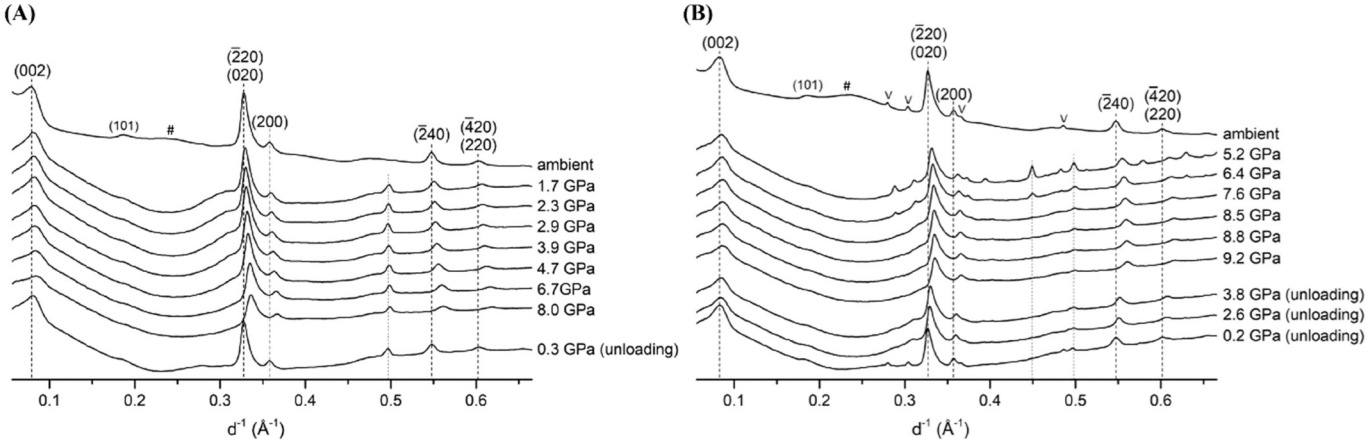

Fig. 5. X-ray diffractograms of non-cross-linked C-A-S-H samples at Ca/Si = 1.0 at different pressures A) for Al/Si = 0.05; B) Al/Si = 0.1. V: vaterite (<1 wt%). Diffractions from the gasket and ruby is indicated with red dot lines. # diffraction of glass capillary. Black dashed lines indicate the peak shifts for guiding the eye. (For interpretation of the references to colour in this figure legend, the reader is referred to the web version of this article.)

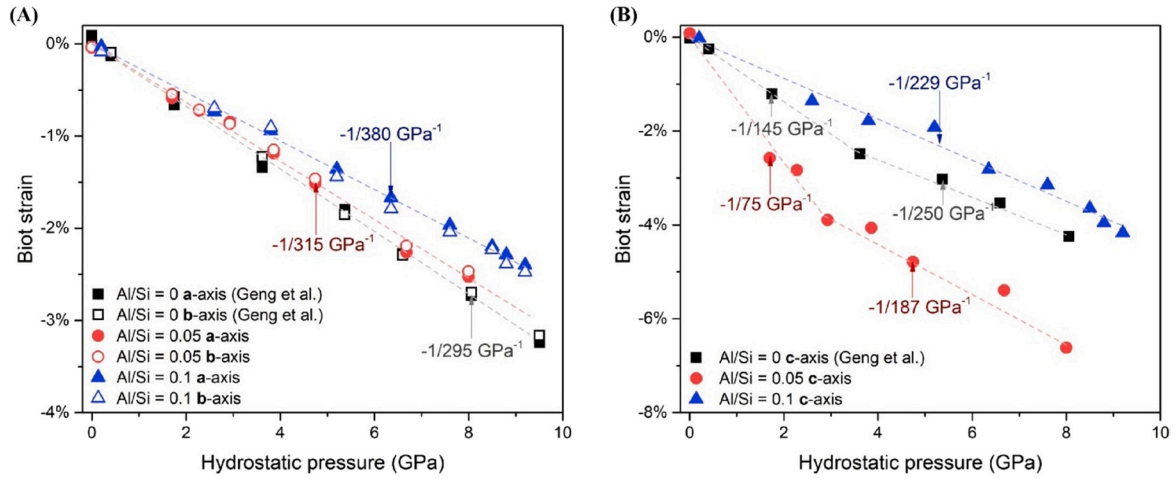

Fig. 6. Biot strain of C-S-H and non-cross-linked C-A-S-H at Ca/Si = 1 as a function of applied hydrostatic pressure A) along the a- and b-axes; B) along the c-axis. The pressure error is <±0.15 GPa, and Biot strain error is <±0.25 %.

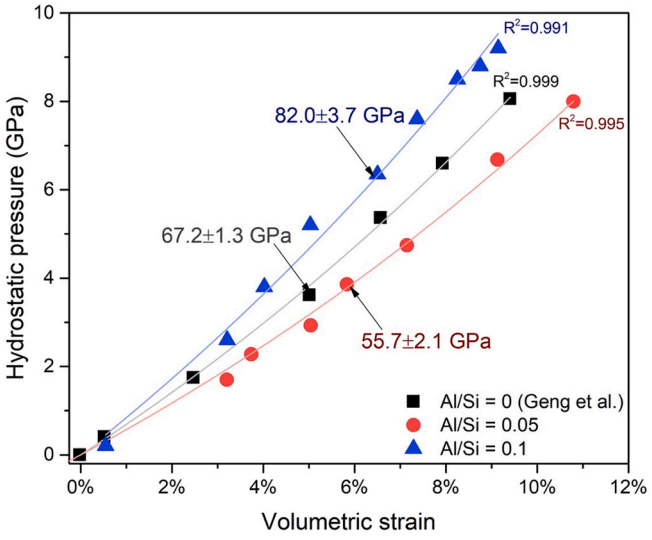

Fig. 7. Applied hydrostatic pressure as a function of volumetric strain of unit cells of non-cross-linked C-A-S-H and C-S-H at Ca/Si = 1 [39]. The pressure error is <±0.15 GPa, and the volumetric strain error is <±0.07 %.

the mechanical properties of each phase at the unit cell scale. K_0 of 20 °C-cured non-cross-linked C-A-S-H at Al/Si = 0.1, 82 ± 4 GPa, is also higher than that of 80 °C-cured cross-linked C-A-S-H at Al/Si = 0.1, 71 ± 3 GPa [38] due to the aforementioned stiffer ab-plane of this non-cross-linked C-A-S-H. Our experimental results of K_0 of non-cross-linked C-A-S-Hs are much higher than the computation results from a density functional theory calculation, 43 GPa [66]. The lower value in the computational study may be due to the higher simulated basal spacing (possibly lower interlayer density). Our experimental results are also higher than K_0 reported in a molecular dynamics study [9], where the values for C-A-S-H, with Na charge-balanced Al, range from 35 to 41 GPa.

The influences of curing age-induced metastability on the structure and mechanical properties of C-A-S-H deserve attention. Besides pore sizes, the interpretation of micromechanical properties of C-A-S-H should not ignore the phase stability in nanoindentation studies [28,67]. Lower Al content or a longer curing age necessitates a stable C-A-S-H system at room temperature. A metastable C-A-S-H sample may partially contribute to the lower nanomechanical properties relative to C-S-H [30]. The stability (e.g., basal spacing, ion concentration, and Al species) of C-A-S-Hs must be investigated to draw solid conclusions regarding the influences of Al on mechanical properties in nanoindentation.

4. Conclusions

This study has investigated the correlation between the structure and nanomechanical properties of non-cross-linked C-A-S-Hs with Ca/Si = 1 synthesized at 20 °C. The nanostructure and nanomechanical properties of non-cross-linked C-A-S-Hs are sensitive to curing-age-related structural (meta)stability. The highly debated TAH [42] is not found in the samples under such conditions. In stable C-A-S-H equilibrated for 546 days, all Al is four-fold coordinated at Al/Si = 0.1. The incorporation of purely Al^{IV} in C-A-S-H (Al/Si = 0.1) results in its higher incompressibility along all axes compared to C-S-H at the same Ca/Si ratio and cured at the same temperature. The Al^{IV}-uptake-induced expansion of basal spacing in the stable C-A-S-H (Al/Si = 0.1) does not lower the c-axis incompressibility. The Al^{IV}-uptake-induced additional charge-balanced Ca results in a higher interlayer density of C-A-S-H at Al/Si = 0.1.

In non-cross-linked C-A-S-H cured for 182 days at Al/Si of 0.05, the system is not fully equilibrated. Al^{IV} is the primary environment among all the Al species, followed by a small fraction of Al^{V} and katoite/AFm-Al^{VI}. The short-curing-induced metastable nanostructure of non-cross-linked C-A-S-H at Al/Si = 0.05 compromises the stiffening effect of Al^{IV}. The ab-planar (basal plane) incompressibility of metastable non-cross-linked C-A-S-H at Al/Si = 0.05 incorporated with Al^{IV} and Al^{V} is just comparable to that of C-S-H at the same Ca/Si ratio. The metastable non-cross-linked C-A-S-H at Al/Si = 0.05 has a 1.5 Å larger basal spacing and fewer charge-balancing Ca for Al at a lower Al/Si ratio, thus lower interlayer density. Thus, the c-axis incompressibility of non-cross-linked C-A-S-H at Al/Si = 0.05 is lower than C-S-H at a comparable Ca/(Al + Si) ratio. The bulk moduli of non-cross-linked C-A-S-H at Al/Si ratios of 0.1 and 0.05 are 82 ± 4 GPa (stable) and 56 ± 2 GPa (metastable), respectively. This study presents the significant negative influence of short-curing-induced metastability on the intrinsic mechanical properties of non-cross-linked C-A-S-H at 182 days, particularly a softer c-axis (softer interlayer). The short curing age plays an important role in forming a metastable local structure in C-A-S-H with inferior intrinsic mechanical properties. A longer curing age favors a stable C-A-S-H structure with superior intrinsic mechanical properties. In practical applications, a longer curing age or faster reaction may enforce the formation of Al^{IV} at low Ca/Si ratios in a stabilized system. The optimization of compositions of blended cement or alkali-activated materials is also important for the formation of stabilized non-cross-linked C-A-S-H.

The experimental results of nanomechanical properties of non-cross-

linked C-A-S-Hs are highly relevant to blended Portland cement-based materials and alkali-activated materials. The experimental results also provide valuable information for computational studies of non-cross-linked C-A-S-Hs. Different C-A-S-H modeling structures and associated modeling parameters and/or simulation methods (e.g., using different force fields) can be optimized and validated accordingly. The sole role of Al^{V} in nanomechanical properties of equilibrated C-A-S-H requires further investigations. The decoupled influences of stabilized Al^{IV} and Al^{V} local structure on the intrinsic mechanical properties of C-A-S-H are still challenging but deserve attention in future studies.

CRediT authorship contribution statement

Jiaqi Li: Conceptualization, Methodology, Investigation, Validation, Visualization, Writing – original draft, Funding acquisition. **Wenxin Zhang:** Investigation, Visualization, Writing – review & editing. **Paula Sanz-Camacho:** Investigation, Visualization, Writing – review & editing. **Mathieu Duttine:** Investigation, Visualization, Writing – review & editing. **David Gardner:** Investigation, Visualization, Writing – review & editing. **Carlo Carraro:** Visualization, Writing – review & editing. **Roya Maboudian:** Validation, Writing – review & editing, Funding acquisition. **Thomas Huthwelker:** Validation, Writing – review & editing.

Declaration of competing interest

The authors declare that they have no known competing financial interests or personal relationships that could have appeared to influence the work reported in this paper.

Acknowledgements

This work was partially performed under the auspices of the U.S. Department of Energy by Lawrence Livermore National Laboratory under Contract DE-AC52-07NA27344. This study is funded by the US National Science Foundation under the Division of Materials Research Ceramics Program, DMR-CER, grant # 1935604. This work is further supported by the Republic of Singapore National Research Foundation through a grant to the Berkeley Education Alliance for Research in Singapore (BEARS) for the Singapore-Berkeley Building Efficiency and Sustainability in the Tropics (SinBerBEST) Program. We thank Dr. Lothenbach for providing the samples synthesized by Dr. L'Hôpital at the Laboratory for Concrete & Construction Chemistry (EMPA). We thank Dr. Paulo Monteiro at UC Berkeley for sharing the beamtime. The Advanced Light Source is supported by the Director, Office of Science, Office of Basic Energy Sciences, of the U.S. Department of Energy under Contract No. DE-AC02-05CH11231. Beamline 12.2.2 is partially supported by COMPRES, the Consortium for Materials Properties Research in Earth Sciences under NSF Cooperative Agreement EAR 1606856. We thank the support from Dr. Andrew Doran, Dr. Jinyuan Yan, and Dr. Martin Kunz at the Advanced Light Source. We acknowledge the Paul Scherrer Institut, Villigen, Switzerland for provision of synchrotron radiation beamtime at beamline PHOENIX of the SLS. LLNL IM release number: LLNL-JRNL-836263.

Appendix A. Supplementary data

Supplementary data to this article can be found online at https://doi.org/10.1016/j.cemconres.2022.106900.

References

[1] M.C.G. Juenger, R. Snellings, S.A. Bernal, Supplementary cementitious materials: new sources, characterization, and performance insights, Cem. Concr. Res. 122 (2019) 257–273.
[2] R. Snellings, G. Mertens, J. Elsen, Supplementary cementitious materials, Rev. Mineral. Geochem. 74 (2012) 211–278.
[3] S.A. Miller, Supplementary cementitious materials to mitigate greenhouse gas emissions from concrete: can there be too much of a good thing? J. Clean. Prod. 178 (2018) 587–598.
[4] M.C. Juenger, R. Siddique, Recent advances in understanding the role of supplementary cementitious materials in concrete, Cem. Concr. Res. 78 (2015) 71–80.
[5] J. Li, W. Zhang, C. Li, P.J.M. Monteiro, Eco-friendly mortar with high-volume diatomite and fly ash: performance and life-cycle assessment with regional variability, J. Clean. Prod. 261 (2020), 121224.
[6] C.E. White, L.L. Daemen, M. Hartl, K. Page, Intrinsic differences in atomic ordering of calcium (alumino)silicate hydrates in conventional and alkali-activated cements, Cem. Concr. Res. 67 (2015) 66–73.
[7] A. Palomo, P. Monteiro, P. Martauz, V. Bilek, A. Fernandez-Jimenez, Hybrid binders: a journey from the past to a sustainable future (opus caementicium futurum), Cem. Concr. Res. 124 (2019), 105829.
[8] J.L. Provis, Alkali-activated materials, Cem. Concr. Res. 114 (2018) 40–48.
[9] F. Puertas, M. Palacios, H. Manzano, J.S. Dolado, A. Rico, J. Rodriguez, A model for the C-A-S-H gel formed in alkali-activated slag cements, J. Eur. Ceram. Soc. 31 (2011) 2043–2056.
[10] X. Zhu, M. Zhang, Y. Yang, K. Yang, F. Wu, Q. Li, L. Yu, C. Yang, M. Basheer, Understanding the aqueous phases of alkali-activated slag paste under water curing, Adv. Cem. Res. 33 (2021) 59–73.
[11] X. Ke, S.A. Bernal, J.L. Provis, Controlling the reaction kinetics of sodium carbonate-activated slag cements using calcined layered double hydroxides, Cem. Concr. Res. 81 (2016) 24–37.
[12] R. Taylor, I.G. Richardson, R.M.D. Brydson, Composition and microstructure of 20-year-old ordinary Portland cement-ground granulated blast-furnace slag blends containing 0 to 100% slag, Cem. Concr. Res. 40 (2010) 971–983.
[13] J. Li, G. Geng, R. Myers, Y.S. Yu, D. Shapiro, C. Carraro, R. Maboudian, P.J. M. Monteiro, The chemistry and structure of calcium (alumino) silicate hydrate: a study by XANES, ptychographic imaging, and wide- and small-angle scattering, Cem. Concr. Res. 115 (2019) 367–378.
[14] C. Rossler, F. Steiniger, H.M. Ludwig, Characterization of C-S-H and C-A-S-H phases by electron microscopy imaging, diffraction, and energy dispersive X-ray spectroscopy, J. Am. Ceram. Soc. 100 (2017) 1733–1742.
[15] P.K. Mehta, P.J. Monteiro, Concrete Microstructure, Properties And Materials, McGraw-Hill, New York, 2017.
[16] S. Merlino, E. Bonaccorsi, A.R. Kampf, Tobermorite 14 angstrom: crystal structure and OD character, Appl. Mineral. 1 and 2 (2000) 859–861.
[17] I.G. Richardson, Model structures for C-(A)-SH (I), Acta Crystallogr. Sect. B: Struct. Sci. Cryst. Eng. Mater. 70 (2014) 903–923.
[18] H. Manzano, J.S. Dolado, M. Griebel, J. Hamaekers, A molecular dynamics study of the aluminosilicate chains structure in Al-rich calcium silicate hydrated (C-S-H) gels, Phys. Status Solidi A 205 (2008) 1324–1329.
[19] R.J. Myers, E. L'Hopital, J.L. Provis, B. Lothenbach, Effect of temperature and aluminium on calcium (alumino)silicate hydrate chemistry under equilibrium conditions, Cem. Concr. Res. 68 (2015) 83–93.
[20] M.D. Andersen, H.J. Jakobsen, J. Skibsted, Incorporation of aluminum in the calcium silicate hydrate (C-S-H) of hydrated Portland cements: a high-field Al-27 and si-29 MAS NMR investigation, Inorg. Chem. 42 (2003) 2280–2287.
[21] M.D. Andersen, H.J. Jakobsen, J. Skibsted, A new aluminium-hydrate species in hydrated Portland cements characterized by 27 Al and 29 Si MAS NMR spectroscopy, Cem. Concr. Res. 36 (2006) 3–17.
[22] M.D. Andersen, H.J. Jakobsen, J. Skibsted, Characterization of white Portland cement hydration and the C-S-H structure in the presence of sodium aluminate by Al-27 and si-29 MAS NMR spectroscopy, Cem. Concr. Res. 34 (2004) 857–868.
[23] G. Renaudin, J. Russias, F. Leroux, C. Cau-dit-Coumes, F. Frizon, Structural characterization of C-S–H and C–A–S–H samples—part II: local environment investigated by spectroscopic analyses, J. Solid State Chem. 182 (2009) 3320–3329.
[24] X. Pardal, F. Brunet, T. Charpentier, I. Pochard, A. Nonat, 27Al and 29Si solid-state NMR characterization of calcium-aluminosilicate-hydrate, Inorg. Chem. 51 (2012) 1827–1836.
[25] M.J.A. Qomi, F.J. Ulm, R.J.M. Pellenq, Evidence on the dual nature of aluminum in the calcium-silicate-hydrates based on atomistic simulations, J. Am. Ceram. Soc. 95 (2012) 1128–1137.
[26] G. Sun, J.F. Young, R.J. Kirkpatrick, The role of Al in C-S–H: NMR, XRD, and compositional results for precipitated samples, Cem. Concr. Res. 36 (2006) 18–29.
[27] A. Kunhi Mohamed, P. Moutzouri, P. Berruyer, B.J. Walder, J. Siramanont, M. Harris, M. Negroni, S.C. Galmarini, S.C. Parker, K.L. Scrivener, L. Emsley, P. Bowen, The atomic-level structure of cementitious calcium aluminate silicate hydrate, J. Am. Chem. Soc. 142 (2020) 11060–11071.
[28] W. Wilson, J.M. Rivera-Torres, L. Sorelli, A. Duran-Herrera, A. Tagnit-Hamou, The micromechanical signature of high-volume natural pozzolan concrete by combined statistical nanoindentation and SEM-EDS analyses, Cem. Concr. Res. 91 (2017) 1–12.
[29] R. Hay, J. Li, K. Celik, Influencing factors on micromechanical properties of calcium (alumino) silicate hydrate C-(A-) SH under nanoindentation experiment, Cem. Concr. Res. 134 (2020), 106088.
[30] W. Hunnicutt, P. Mondal, L. Struble, Dynamic and quasi-static nanoindentation of CSH and CASH, Spec.Publ. 312 (2016) 1–15.
[31] P. Trtik, B. Munch, P. Lura, A critical examination of statistical nanoindentation on model materials and hardened cement pastes based on virtual experiments, Cem. Concr.Compos. 31 (2009) 705–714.
[32] M. Miller, C. Bobko, M. Vandamme, F.J. Ulm, Surface roughness criteria for cement paste nanoindentation, Cem. Concr. Res. 38 (2008) 467–476.

[33] R. Hay, J. Li, K. Celik, Phase evolution, micromechanical properties, and morphology of calcium (alumino) silicate hydrates C-(A-) SH under carbonation, Cem. Concr. Res. 152 (2022), 106683.
[34] J. Li, W. Zhang, P.J. Monteiro, Synchrotron X-ray Raman scattering shows the changes of the Ca environment in CSH exposed to high pressure, Cem. Concr. Res. 132 (2020), 106066.
[35] G. Geng, R.N. Vasin, J. Li, M.J.A. Qomi, J. Yan, H.R. Wenk, P.J.M. Monteiro, Preferred orientation of calcium aluminosilicate hydrate induced by confined compression, Cem. Concr. Res. 113 (2018) 186–196.
[36] J. Li, W. Zhang, P.J. Monteiro, Preferred orientation of calcium aluminosilicate hydrate compacts: implications for creep and indentation, Cem. Concr. Res. 143 (2021), 106371.
[37] J.H. Moon, J.E. Oh, M. Balonis, F.P. Glasser, S.M. Clark, P.J.M. Monteiro, Pressure induced reactions amongst calcium aluminate hydrate phases, Cem. Concr. Res. 41 (2011) 571–578.
[38] G. Geng, R.J. Myers, J. Li, R. Maboudian, C. Carraro, D.A. Shapiro, P.J. Monteiro, Aluminum-induced dreierketten chain cross-links increase the mechanical properties of nanocrystalline calcium aluminosilicate hydrate, Sci. Rep. 7 (2017) 44032.
[39] G. Geng, R.J. Myers, M.J.A. Qomi, P.J.M. Monteiro, Densification of the interlayer spacing governs the nanomechanical properties of calcium-silicate-hydrate, Sci. Rep. 7 (2017) 10986.
[40] J. Li, W. Zhang, P.J.M. Monteiro, The structure and intrinsic mechanical properties of nanocrystalline calcium silicate hydrate, ACS Sustain. Chem. Eng. 8 (2020) 12453–12461.
[41] J. Li, W. Zhang, K. Garbev, G. Beuchle, P.J. Monteiro, Influences of cross-linking and Al incorporation on the intrinsic mechanical properties of tobermorite, Cem. Concr. Res. 136 (2020), 106170.
[42] E. L'Hôpital, B. Lothenbach, G. Le Saout, D. Kulik, K. Scrivener, Incorporation of aluminium in calcium-silicate-hydrates, Cem. Concr. Res. 75 (2015) 91–103.
[43] S. Barzgar, M. Tarik, C. Ludwig, B. Lothenbach, The effect of equilibration time on Al uptake in CSH, Cem. Concr. Res. 144 (2021), 106438.
[44] E. L'Hôpital, B. Lothenbach, K. Scrivener, D. Kulik, Alkali uptake in calcium alumina silicate hydrate(CASH), Cem. Concr. Res. 85 (2016) 122–136.
[45] E. L'Hôpital, B. Lothenbach, D. Kulik, K. Scrivener, Influence of calcium to silica ratio on aluminium uptake in calcium silicate hydrate, Cem. Concr. Res. 85 (2016) 111–121.
[46] J.C. Chervin, B. Canny, M. Mancinelli, Ruby-spheres as pressure gauge for optically transparent high pressure cells, High Pressure Res. 21 (2002) 305–314.
[47] C. Biagioni, S. Merlino, E. Bonaccorsi, The tobermorite supergroup: a new nomenclature, Mineral. Mag. 79 (2015) 485–495.
[48] G. Renaudin, J. Russias, F. Leroux, F. Frizon, C. Cau-dit-Coumes, Structural characterization of C-S–H and C–A–S–H samples—part I: long-range order investigated by Rietveld analyses, J. Solid State Chem. 182 (2009) 3312–3319.
[49] J.-B.d.E. de Lacaillerie, C. Fretigny, D. Massiot, MAS NMR spectra of quadrupolar nuclei in disordered solids: the Czjzek model, J.Magn.Reson. 192 (2008) 244–251.
[50] I. Richardson, J. Skibsted, L. Black, R. Kirkpatrick, Characterisation of cement hydrate phases by TEM, NMR and Raman spectroscopy, Adv. Cem. Res. 22 (2010) 233–248.
[51] D. Li, G.M. Bancroft, M.E. Fleet, X.H. Feng, Silicon K-edge Xanes spectra of silicate minerals, Phys. Chem. Miner. 22 (1995) 115–122.
[52] J. Li, W. Zhang, K. Garbev, P.J. Monteiro, Coordination environment of Si in calcium silicate hydrates, silicate minerals, and blast furnace slags: a XANES database, Cem. Concr. Res. 143 (2021), 106376.
[53] S.J. Naftel, T.K. Sham, Y.M. Yiu, B.W. Yates, Calcium L-edge XANES study of some calcium compounds, J. Synchrotron Radiat. 8 (2001) 255–257.
[54] J. Li, G. Geng, W. Zhang, Y.S. Yu, D.A. Shapiro, P.J.M. Monteiro, The hydration of beta- and alpha(H)'-dicalcium silicates: an X-ray spectromicroscopic study, ACS Sustain. Chem. Eng. 7 (2019) 2316–2326.
[55] G.Q. Geng, R. Taylor, S. Bae, D. Hernandez-Cruz, D.A. Kilcoyne, A.H. Emwas, P.J. M. Monteiro, Atomic and nano-scale characterization of a 50-year-old hydrated C3S paste, Cem. Concr. Res. 77 (2015) 36–46.
[56] J. Li, W. Zhang, K. Xu, P.J.M. Monteiro, Fibrillar calcium silicate hydrate seeds from hydrated tricalcium silicate lower cement demand, Cem. Concr. Res. 137 (2020), 106195.
[57] J. Ha, S. Chae, K.W. Chou, T. Tyliszczak, P.J.M. Monteiro, Scanning transmission X-ray microscopic study of carbonated calcium silicate hydrate, Transp.Res. Rec. (2010) 83–88.
[58] J.E. Oh, S.M. Clark, P.J.M. Monteiro, Does the Al substitution in C-S-H(I) change its mechanical property? Cem. Concr. Res. 41 (2011) 102–106.
[59] D.W. Gardner, J. Li, A. Morshedifard, S. Masoumi, M.J. Abdolhosseini Qomi, P. J. Monteiro, R. Maboudian, C. Carraro, Silicate bond characteristics in calcium-silicate-hydrates determined by high pressure Raman spectroscopy, J. Phys. Chem. C 124 (33) (2020).
[60] M.D. Jackson, S.R. Chae, S.R. Mulcahy, C. Meral, R. Taylor, P. Li, A.-H. Emwas, J. Moon, S. Yoon, G. Vola, Unlocking the secrets of Al-tobermorite in Roman seawater concrete, Am. Mineral. 98 (2013) 1669–1687.
[61] S. Soyer-Uzun, S.R. Chae, C.J. Benmore, H.R. Wenk, P.J.M. Monteiro, Compositional evolution of calcium silicate hydrate (C-S-H) structures by total X-ray scattering, J. Am. Ceram. Soc. 95 (2012) 793–798.
[62] C.E. White, Effects of temperature on the atomic structure of synthetic calcium-silicate-deuterate gels: a neutron pair distribution function investigation, Cem. Concr. Res. 79 (2016) 93–100.
[63] R. Shahsavari, M.J. Buehler, R.J.M. Pellenq, F.J. Ulm, First-principles study of elastic constants and interlayer interactions of complex hydrated oxides: case study of tobermorite and jennite, J. Am. Ceram. Soc. 92 (2009) 2323–2330.
[64] C.W. Burnham, M. Buerger, Refinement of the crystal structure of andalusite, Z. Kristall. 115 (1961) 269–290.
[65] R. Demichelis, B. Civalleri, Y. Noel, A. Meyer, R. Dovesi, Structure and stability of aluminium trihydroxides bayerite and gibbsite: a quantum mechanical ab initio study with the CRYSTAL06 code, Chem. Phys. Lett. 465 (2008) 220–225.
[66] Q. Zheng, J.Y. Jiang, J. Yu, X.L. Li, S.F. Li, Aluminum-induced interfacial strengthening in calcium silicate hydrates: structure,bonding, and mechanical properties, ACS Sustain. Chem. Eng. 8 (2020) 2622–2631.
[67] Z. Jia, C. Chen, H. Zhou, Y. Zhang, The characteristics and formation mechanism of the dark rim in alkali-activated slag, Cem. Concr. Compos. 112 (2020), 103682.
[68] S. Ortaboy, J. Li, G. Geng, R.J. Myers, P.J. Monteiro, R. Maboudian, C. Carraro, Effects of CO 2 and temperature on the structure and chemistry of C–(A–) S-H investigated by Raman spectroscopy, RSC Adv. 77 (2017) 48925–48933.